






Estimating the Evolution of Sparks in the Partially Screened Gap of Pulsars from Subpulse Drifting

Rahul Basu¹ , Dipanjan Mitra^{1,2} , and George I. Melikidze^{1,3} ¹Janusz Gil Institute of Astronomy, University of Zielona Góra, ul. Szafrana 2, 65-516 Zielona Góra, Poland²National Centre for Radio Astrophysics, Tata Institute of Fundamental Research, Pune 411007, India³Evgeni Kharadze Georgian National Astrophysical Observatory, 0301 Abastumani, Georgia

Received 2023 February 22; revised 2023 March 21; accepted 2023 March 21; published 2023 April 26

Abstract

A novel scheme has been developed to show that the observed phase behavior associated with subpulse drifting from two pulsars, J1034–3224 and J1720–2933, can be used to obtain the magnetic field configuration in the partially screened gap (PSG). The outflowing plasma along the open magnetic field line region of pulsars is generated as a result of spark discharges in an inner acceleration region (IAR) above the polar cap. The IAR has been modeled as a PSG with a steady supply of positively charged ions emitted from the heated polar cap surface dominated by strong non-dipolar magnetic fields. In a PSG the sparks are tightly packed and constrained to be present along the polar cap boundary. The sparks lag behind the rotation of the star during their lifetimes. As a result, the sparking pattern evolves along two different directions in a clockwise and counterclockwise manner around a stationary central spark and can be associated with the observed phenomenon of subpulse drifting. PSR J1034–3224 has four prominent components and exhibits bi-drifting where alternate components show the opposite sense of drifting, while PSR J1720–2933 has a single component profile and shows systematically coherent drift bands. We show that the differences in their drifting behavior can be directly linked to different natures of the non-dipolar surface magnetic field configurations.

Unified Astronomy Thesaurus concepts: Pulsars (1306); Radio pulsars (1353)

Supporting material: animations

1. Introduction

A steady outflow of relativistic plasma is set up along the open magnetic field lines of the pulsar magnetosphere. This outflowing plasma forms the pulsar wind and is also the source of coherent radio emission that arises owing to nonlinear plasma instabilities. Detailed observations have shown that the radio emission is emitted close to the surface at heights less than 10% of the light cylinder radius (von Hoensbroech & Xilouris 1997; Kijak & Gil 1998; Mitra & Rankin 2002; Weltevrede & Johnston 2008; Krzeszowski et al. 2009; Mitra 2017). This requires the outflowing plasma to be generated primarily in an inner acceleration region (IAR) above the polar caps. The IAR was initially modeled as an inner vacuum gap, where the gap extended to a height of around 100 m above the surface (Ruderman & Sutherland 1975). The plasma is generated from spark discharges due to cascading electron–positron pair production in the gap, which are subsequently accelerated to relativistic energies in the large potential drop, with the positrons flowing outward and the electrons accelerated backward to heat the surface. The cascading effect requires the surface magnetic field to be highly non-dipolar in nature, while heating from the back-streaming particles raises the surface temperatures above the polar cap to around 10^6 K. The high surface temperatures and presence of non-dipolar fields on the polar cap have been confirmed by observations of X-ray emission from the stellar surface (Gil et al. 2008; Hermsen et al. 2013; Geppert 2017;

Szary et al. 2017; Hermsen et al. 2018; Arumugasamy & Mitra 2019; Pétri & Mitra 2020; Sznajder & Geppert 2020). The surface temperatures are close to the critical level such that the high-energy tail of the distribution of ions can flow freely from the surface and form a partially screened gap (PSG; see Section 2.1 in Gil et al. 2003). In a PSG, spark discharges are a mechanism of regulating the surface temperature around this critical level, and the sparks are constrained to be arranged around the polar cap boundary. The sparks are formed in a tightly packed configuration across the cross section of the polar cap and lag behind the rotation of the pulsar owing to ExB drift in the gap (Basu et al. 2020; Mitra et al. 2020; Basu et al. 2022).

The phenomenon of subpulse drifting, seen in the single pulse sequence of several pulsars, reflects the drift behavior of the sparks (Weltevrede et al. 2006; Basu et al. 2016; Song et al. 2023) and provides a direct probe into the physical processes within the IAR. The drifting behavior is measured using the longitude-resolved fluctuation spectrum (LRFS) analysis, where Fourier transforms of the pulse sequence are carried out along several narrow longitude ranges within the emission window to characterize the periodic behavior (Backer 1973). The primary measurements are the drifting periodicity, P_3 , which can be related to the electric potential difference in the IAR, and the phase variations across the emission window, which follows the evolution of the sparking pattern in the non-dipolar polar cap along the observers' line of sight (LOS). The drifting phase behavior shows different patterns ranging from systematic change across the profile to phase shifts in different components (Basu et al. 2019a). The most remarkable behavior is seen in a small category of pulsars that exhibit bi-drifting, where the drifting phases show reversal in directions in

Table 1
Radio Emission Properties and Line-of-sight Geometry

PSR	P (s)	\dot{P} (s s ⁻¹)	ν (MHz)	W_C (deg)	$W_{5\sigma}$ (deg)	W_B (deg)	R_{ppa} (deg)	α (deg)	α_m (deg)	β (deg)	ρ (deg)	S_{los}	h (km)
J1034–3224	1.15	2.3×10^{-16}	325	7.4 ± 0.9	80.2 ± 1.8	2.37	9.95	17.4 ± 2.0	16.6/163.4	± 1.6	11.9	± 0.14	1073
			610	7.1 ± 0.2	68.9 ± 0.4	2.16		16.5 ± 0.5		10.3	± 0.16	806	
J1720–2933	0.62	7.5×10^{-16}	325	5.0 ± 0.2	25.7 ± 0.4	2.37	–6.6	37.1 ± 1.7	38.3/141.7	± 5.4	9.2	± 0.59	348
			610	4.2 ± 0.2	24.1 ± 0.4	2.16		40.3 ± 2.3		8.8	± 0.61	320	

different components of the profile (Champion et al. 2005; Weltevrede 2016; Szary & van Leeuwen 2017; Basu & Mitra 2018; Basu et al. 2019b; Szary et al. 2020; Shang et al. 2022).

Modeling the observed drifting phase behavior requires estimating the surface magnetic field configuration that determines the polar cap structure and the temporal evolution of the sparking pattern in the IAR above the polar cap. Basu et al. (2022) showed that in a PSG the sparking pattern is constrained by the boundary of the polar cap to evolve around concentric rings in a direction opposite to the rotation of the pulsar. Although the individual sparks have much shorter durations than the drifting periodicity, the subsequent sparks are formed shifted in either a clockwise or counterclockwise manner around a stationary spark at the center, and the overall sparking pattern mimics a drift behavior. The non-dipolar surface magnetic field configuration, on the other hand, is less well understood. Gil et al. (2002) suggested a simple approximation consisting of a star-centered dipole and a weaker local dipole on the surface that determines the surface field.

In this work we have used the measured drifting behavior from two pulsars J1034–3224 and J1720–2933 (Basu & Mitra 2018) with different characteristics, to estimate the spark behavior in the PSG and the surface magnetic field configuration. PSR J1034–3224 has four prominent components in the average profile and shows the bi-drifting behavior with alternate components having opposite drift directions. PSR J1720–2933 has a single component profile and shows systematic drifting with large monotonic phase variations. These studies provide observational validation of the PSG model and give an outline for estimating the physical properties of IAR in pulsars. In Section 2 we report the estimates of LOS geometry from the observations in both pulsars, while Section 3 details the estimation of spark evolution in the PSG and the nature of surface magnetic fields in order to reproduce the observed drifting behavior. We summarize our results and briefly discuss the application of these studies in the larger pulsar population in Section 4.

2. Radio Emission Properties

PSR J1034–3224 and PSR J1720–2933 were observed as part of the Meterwavelength Single Pulse Emission Survey (MSPES; Mitra et al. 2016) conducted using the Giant Meterwave Radio Telescope. Around 2000 polarized single pulses were observed in this survey at two separate frequencies of 325 and 610 MHz. Subsequently, longer observations were carried out by Basu & Mitra (2018) at 325 MHz to characterize the drifting features in each pulsar. The drifting behavior of the sparks is imprinted on the outflowing plasma, which gives rise to the radio emission at heights of several hundred kilometers

from the surface, where the magnetic field is dipolar in nature. Hence, it is imperative to understand the dipolar geometry of the radio emission region to unravel the spark evolution in the IAR.

The quantities used to specify the geometry include the inclination angle between the rotation and magnetic axis, α , the angle at the closest approach of the LOS to the magnetic axis, β , the emission height at a given frequency (ν), h_ν , the beam opening angle at that frequency, ρ_ν , and the relative LOS traverse across the emission beam, $S_{\text{los}} = \beta/\rho_\nu$. The inclination angle can be obtained from the width of the profile components as (Skrzypczak et al. 2018)

$$W_C = W_B P^{-0.5} / \sin \alpha. \quad (1)$$

Here W_C is the half-width of the component in the profile at the observing frequency. The distribution of the component widths as a function of period (P), at any given frequency, is seen to be above a lower boundary line that is specified by the width parameter, W_B . The above estimate has a degeneracy between α and $\pi - \alpha$. The angles α and β can be estimated from rotating vector model (RVM; Radhakrishnan & Cooke 1969) fits to polarization position angle (PPA). However, these yield correlated values that are unreliable, and only the steepest gradient point (R_{ppa}) of the PPA can be used to constrain the geometry as (Mitra & Li 2004)

$$R_{\text{ppa}} = |\sin \alpha / \sin \beta|. \quad (2)$$

The beam opening angle can be estimated from the full width of the pulsar profile, $W_{5\sigma}$, which is assumed to be connected with the last open field lines, using spherical geometry (Gil et al. 1984):

$$\sin^2(\rho_\nu/2) = \sin \alpha \sin(\alpha + \beta) \sin^2(W_{5\sigma}/4) + \sin^2(\beta/2). \quad (3)$$

The beam opening angle can be further used to estimate the radio emission height

$$h_\nu = 10P \left(\frac{\rho_\nu}{1.23} \right)^2 \text{ km}, \quad (4)$$

where the beam opening angle at a distance of 10 km for the dipolar field lines is $1^\circ 23'$, for $P = 1$ s.

Table 1 shows the estimates of geometry and emission heights at 325 and 610 MHz for the two pulsars J1034–3224 and J1720–2933. The profile and component widths at both frequencies were estimated in Skrzypczak et al. (2018), which also reported the estimate of W_B from the distribution of the widths. The PPAs were reported in Mitra et al. (2016), and we carried out RVM fits to obtain R_{ppa} for each pulsar (the detailed RVM fitting process for the pulsars in the MSPES survey, including the two reported here, is shown in Mitra et al. 2023, in preparation). The α values obtained independently at the two

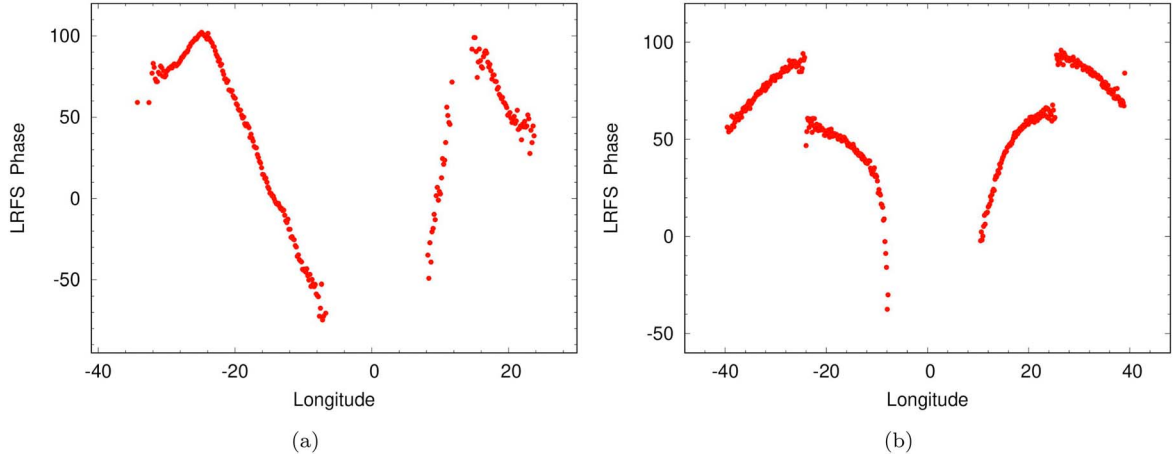


Figure 1. (a) The observed phase behavior associated with subpulse drifting in PSR J1034–3224, reported in Basu & Mitra (2018). The pulsar has four profile components, and the subpulse drifting shows the rare bi-drifting nature in this pulsar. The first and third components have positive slopes in the phase variations, while the second and fourth components have negative slopes. The two inner components have steeper slopes compared to the two outer ones. The phases in the first two components have been shifted by $+180^\circ$, while the third component has been shifted by -180° to provide optimum range along the y-axis for highlighting the bi-drifting behavior in this pulsar. (b) The estimated phase behavior associated with subpulse drifting in a simulated single pulse sequence is shown. The phase variations reproduce the primary features seen in PSR J1034–3224, including the bi-drifting nature and the relative slope changes between the inner and outer components.

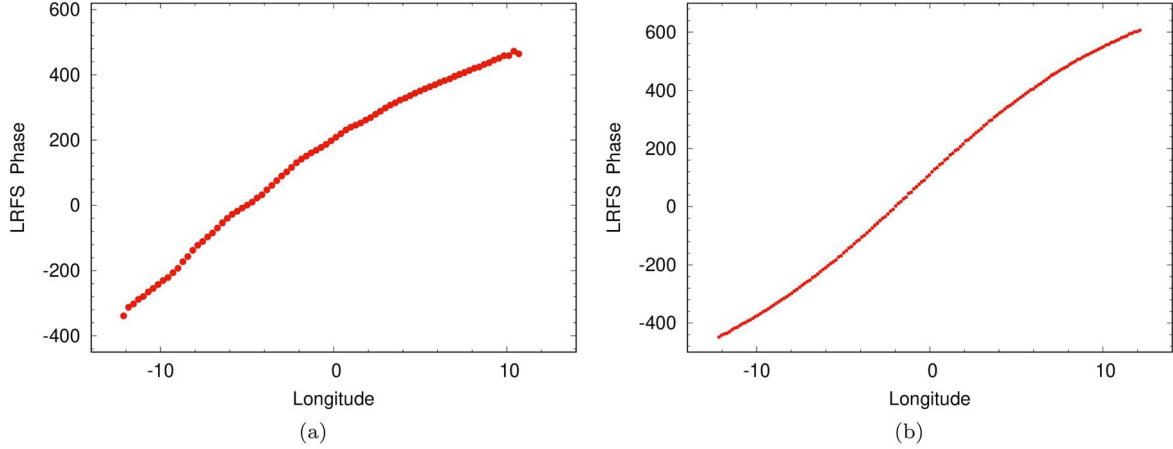


Figure 2. (a) The observed phase behavior associated with subpulse drifting in PSR J1720–2933, reported in Basu & Mitra (2018). The phases show large variations across the profile with a positive slope across the phase window. (b) The estimated phase behavior associated with subpulse drifting in a simulated single pulse sequence is shown. The phase variations exhibit the general observed behavior seen in PSR J1720–2933.

Table 2
The Physical Parameters of the Partially Screened Gap

	a_{cap} (m)	b_{cap} (m)	θ_{cap} (deg)	θ_{cap}^c (deg)	ϕ_{cap}^c (deg)	$b = B_s/B_d$	$ \cos \alpha_i $	η	h_\perp (m)	T_i (10^6 K)	ΔV_{PSG} (10^{10} V)
J1034–3224	36.2	15.1	–45.5	166.5	–48.8	~ 67	~ 0.65	0.034	4.3	1.17	1.56
J1720–2933	75.2	30.1	–36.8	37.1	20.9	~ 32	~ 0.25	0.26	8.8	3.93	22.4

frequencies are consistent within measurement errors, and a weighted mean α_m is used for estimating the other parameters.

3. Estimating Properties of the Partially Screened Gap from Subpulse Drifting

The surface magnetic field configuration is approximated by considering the presence of a dominant star-centered dipole and one or more weaker dipoles located just below the stellar surface (Gil et al. 2002), such that the magnetic field becomes dipolar a few kilometers away from the surface. The polar cap configuration is determined by the relative strength and

location of the surface dipoles. The presence of subpulse drifting suggests that the polar cap has a relatively smooth boundary and can be approximated to have an elliptical shape with major axis a_{cap} , minor axis b_{cap} , and inclination angle θ_{cap} in a given coordinate plane. The center of the polar cap on the neutron star surface is located at $(R_S, \theta_{\text{cap}}^c, \phi_{\text{cap}}^c)$, in the rotating coordinate system with the neutron star at the center and the rotation axis aligned along the z-axis. Here $R_S = 10^6$ cm is the radius of the neutron star. For a given polar cap, the spark sizes are constrained from average emission beam studies that have been shown to comprise a central core component surrounded

by two concentric rings of conal emission (Rankin 1993; Mitra & Deshpande 1999; see also Appendix A). The sparks are expected to have an elliptical shape resembling the polar cap, specified by major axis a_{spark} and minor axis b_{spark} , with effective size $h_{\perp} \sim \sqrt{a_{\text{spark}} b_{\text{spark}}}$. A detailed characterization of the PSG can be achieved from the drifting periodicity P_3 and the non-dipolar surface fields in the polar cap characterized by the parameters $b = B_s/B_d$, with B_s being the non-dipolar field strength and B_d the global dipolar field, and α_l , the angle made by the local non-dipolar magnetic field with the rotation axis (Mitra et al. 2020; Basu et al. 2022). The screening factor η of the potential drop in a PSG is obtained as

$$\eta = 1/(2\pi P_3 |\cos \alpha_l|). \quad (5)$$

The electric potential difference in the gap can be estimated as

$$\Delta V_{\text{PSG}} = \frac{4\pi\eta b B_d |\cos \alpha_l| h_{\perp}^2}{Pc}, \quad (6)$$

and the surface temperature of the polar cap, which corresponds to the critical temperature T_i , is

$$T_i = (\eta b)^{1/2} |\cos \alpha_l|^{1/4} \left(\frac{h_{\perp}}{2.6 \text{ m}} \right)^{1/2} \left(\frac{\dot{P}_{-15}}{P} \right)^{1/4} \times 10^6 \text{ K}. \quad (7)$$

Here \dot{P}_{-15} is the period derivative in units of $10^{-15} \text{ s s}^{-1}$. A detailed scheme of estimating the sparking pattern evolution in the PSG and the corresponding subpulse drifting behavior for a specific surface field configuration has been discussed in Basu et al. (2020, 2022). We would like to emphasize that in this work we are concerned with inverting the problem to obtain constraints for the surface magnetic field from the observed drifting behavior.

The magnetic field configuration is modeled using a combination of a global dipole located at the origin and one or more local crust-anchored dipoles (Gil et al. 2002). The global dipole is oriented in the x - z plane and specified as $d = (d, \theta_d, 0^\circ)$, where $d = B_d R_S^3$, $B_d = 10^{12} (P\dot{P}_{-15})^{0.5} \text{ G}$, and $\theta_d = \alpha$, obtained from Equation (1). The crust-anchored dipoles, which are less well constrained, with dipole moments $m_i = (m^i, \theta_m^i, \phi_m^i)$, where $i = 1, 2, \dots$, are located at $r_i = (r_s^i, \theta_s^i, \phi_s^i)$ just below the surface. Although it is likely that a number of effective dipoles exist near the surface, the non-dipolar polar cap is expected to be formed around one dominant dipole. Observations of X-ray emission from the surface of a number of pulsars show the magnetic field strength to be in the range $b \sim 10$ – 100 (Geppert 2017; Sznajder & Geppert 2020). The magnetic field lines from the non-dipolar polar cap surface connect with the dipolar field in the emission region at a height $h_p \sim 100$ – 1000 km from the surface. Depending on the relative orientation of the polar cap, the LOS gets twisted and can have different cuts on the surface for the same emission geometry, specified by α and β . The phase variations associated with drifting, which measures the delay between the spark peaks along the LOS cut of the polar cap surface, exhibit a unique behavior for every different orientation of the surface dipole.

We have carried out a numerical search for the surface magnetic field configuration of the two pulsars J1034–3224 and J1720–2933. The parameters of m and r were varied to obtain different realizations of the polar cap. The drifting phase behavior for the LOS geometry in each polar cap was estimated and subsequently compared with the measured drifting

behavior to find unique solutions. We fixed $m = 0.01d$ and $r_s = 0.95R_S$ to ensure the appropriate range of b and also reduce the parameter space for the search. The results of the polar cap fits and the corresponding PSG properties in each pulsar are presented below.

PSR J1034–3224. The pulsar has four primary components in the profile, as well as a precursor that becomes prominent at higher frequencies above 600 MHz (Basu et al. 2015). The observed radio emission properties and the estimated LOS geometry are shown in Table 1. Subpulse drifting is seen in the four components of the profile with drifting periodicity $P_3 = 7.2 \pm 0.7P$, and the phase variations exhibit bi-drifting behavior (see Figure 1(a); Basu & Mitra 2018). The first and third components show positive slope in their phase variations, while the second and fourth components have negative slopes. The phase variations are steeper by roughly a factor of two in the inner components compared with the outer ones. We obtained the best-fit surface magnetic field configuration to reproduce the bi-drifting behavior in this pulsar to be $m = (0^\circ 01d, 165^\circ 9, 312^\circ 0)$, located at $r = (0^\circ 95R_S, 133^\circ 5, 237^\circ)$ for the emission geometry specified by $\alpha = 163^\circ 4$ and $\beta = 1^\circ 6$. The details of the polar cap parameters for this configuration, as well as the spark distribution in the PSG, are reported in Table 2 and Appendix A. A sequence of 200 single pulses were simulated for this configuration (see Basu et al. 2022; see also Appendix B), and the LRFS was estimated for this sequence. The phase behavior of the LRFS is shown in Figure 1(b) and reproduces the primary features of the bi-drifting behavior seen in this pulsar.

PSR J1720–2933. The pulsar has one broad component in the profile with a dip at the center and shows systematic coherent drifting across the emission window. The drifting periodicity is $P_3 = 2.45P$, and the phases show large monotonic variations and slight flattening toward the trailing edge (see Figure 2(a); Basu & Mitra 2018). The observed radio emission properties and the estimated LOS geometry are shown in Table 1. We obtained the best-fit surface magnetic field configuration to be $m = (0^\circ 01d, 36^\circ 3, 24^\circ 0)$, located at $r = (0^\circ 95R_S, 52^\circ 0, 45^\circ 0)$ for the emission geometry specified by $\alpha = 38^\circ 3$ and $\beta = -5^\circ 4$. The details of the polar cap parameters for this configuration, as well as the spark distribution in the PSG, are reported in Table 2 and Appendix A. We estimated the LRFS for a sequence of 200 single pulses that were simulated for the above configuration (see Basu et al. 2022; see also Appendix B). The phase behavior of the LRFS is shown in Figure 2(b) and reproduces the general coherent drifting behavior of this pulsar.

4. Summary and Conclusion

We have used the subpulse drifting behavior from two contrasting examples of PSR J1034–3224 and PSR J1720–2933 to demonstrate that the evolution of the spark distribution predicted by the PSG model of the IAR can be used to understand the nature of this difference. There are two primary factors that determine phase variations associated with subpulse drifting, the LOS geometry and the orientation of the polar cap over which the sparking pattern evolves. The LOS geometry determines the number of components in the average profile, with single- and double-component profiles associated with outer LOS cuts across the emission beam with $|S_{\text{los}}| > 0.5$, while four- or five-component profiles are seen in central cuts with $|S_{\text{los}}| < 0.2$. The systematic coherent drift is usually seen

in pulsars with single- and double-component profiles, while phase shifts and reversals are associated with profiles having both inner and outer conal components (Basu et al. 2019a). The LOS cut across the emission region is altered during transition to the non-dipolar polar cap. The exact phase behavior is determined by the effective LOS traverse across the polar cap and traces its relative orientation. We have used the drifting phase variations in the two pulsars to constrain the nature of the polar cap and the surface magnetic field configuration of the two pulsars. This allowed us to estimate the physical properties of the PSG and the spark distribution. Due to multiple parameters involved in specifying the surface dipole configuration, the solutions reported here are not unique, and there are other possible setups that can give similar drifting phase behavior. But many of these solutions lead to unphysical results, like the polar cap being highly extended along an axis or having much higher b value and located much farther from the dipolar polar cap, and can be discarded as likely solutions. The X-ray observations of the stellar surface coupled with the drifting phase behavior would enable tighter constraints on these estimations of the surface magnetic fields in neutron stars.

D.M. acknowledges the support of the Department of Atomic Energy, Government of India, under project no. 12-R&D-TFR-5.02-0700. D.M. acknowledges funding from the ‘‘Indo-French Centre for the Promotion of Advanced Research—CEFIPRA’’ grant IFC/F5904-B/2018. This work was supported by grant 2020/37/B/ST9/02215 of the National Science Centre, Poland.

Appendix A

Estimating the Nature of the Polar Cap and the Sparking Distribution

Figure 3 shows the variations of the magnetic fields across the polar cap surface. Figures 3(a) and (c) correspond to the parameter b , which specifies the relative strength of the surface field, while Figures 3(b) and (d) show $|\cos \alpha_l|$, which shows the local inclination of the magnetic field. Both these quantities determine the screening factor, the surface temperature, and the potential difference in PSG estimated in Table 2.

The two-dimensional distribution of the sparks and their evolution with time in PSR J1034–3224 is shown in the animated Figure 4, along with the LOS cut across the cap that results in the observed bi-drifting behavior. The animated

Figure 5 shows the spark distribution in the polar cap of PSR J1720–2933, along with the LOS geometry that gives rise to the coherent drifting behavior. In each case we have considered two concentric rings for the spark evolution around a centrally localized spark, which evolve in two separate directions in a clockwise and counterclockwise manner, respectively. The bi-drifting behavior requires the LOS to cut across both these tracks in both directions of evolution in an appropriate manner. The coherent drifting on the other requires the LOS to only follow the outer track along one direction.

Table 3 reports the different parameters that describe the distribution of sparks in each polar cap (see Basu et al. 2022, for a more detailed description). The sparks are tightly packed in the IAR and arranged in concentric rings around a central spark. The observations of the average beam properties show the presence of two pairs of conal components surrounding a central core that constrains the typical number of such tracks to be $N_{\text{trk}} = 2$. The maximum packing condition specifies the size of the sparks to be $N_{\text{trk}} = \text{Int}(a_{\text{cap}}/a_{\text{sprk}}) = \text{Int}(b_{\text{cap}}/b_{\text{sprk}})$. In an elliptical polar cap the tracks are bound by the ellipses defined by $a_{\text{out}}^i, b_{\text{out}}^i$ and $a_{\text{in}}^i, b_{\text{in}}^i$, where $i = 1, 2$, corresponding to the outer and inner conal tracks, respectively. The maximum number of fully formed sparks along each conal track is N_{sprk}^i , and these quantities can be estimated as

$$\begin{aligned} a_{\text{out}}^i &= a_{\text{cap}} - 2(i-1)a_{\text{sprk}}, & a_{\text{in}}^i &= a_{\text{out}}^i - 2a_{\text{sprk}}, \\ b_{\text{out}}^i &= b_{\text{cap}} - 2(i-1)b_{\text{sprk}}, & b_{\text{in}}^i &= b_{\text{out}}^i - 2b_{\text{sprk}}, \\ N_{\text{sprk}}^i &= \text{Int}(F(a_{\text{out}}^i b_{\text{out}}^i - a_{\text{in}}^i b_{\text{in}}^i)/(a_{\text{sprk}} b_{\text{sprk}})). \end{aligned} \quad (\text{A1})$$

Here F is a scaling factor for maximum packing, which was found to be around 0.75. The angular size of the sparks in each track is $\theta_{\text{sprk}}^i = 2\pi/N_{\text{sprk}}^i$, and their centers lie on the ellipse specified by $a_{\text{trk}}^i = (a_{\text{out}}^i + a_{\text{in}}^i)/2$ and $b_{\text{trk}}^i = (b_{\text{out}}^i + b_{\text{in}}^i)/2$.

In order to estimate the two-dimensional spark distribution, a Cartesian $x'y'$ -plane is defined to contain the elliptical polar cap with origin at the center of the ellipse. The boundary of the upper and lower halves of the polar cap signifying clockwise and anticlockwise evolution of the sparking pattern is specified by the angles $\theta'_s = \pi/2 - \phi_{\text{cap}}^c$ and $\theta'_e = 3\pi/2 - \phi_{\text{cap}}^c$, where θ' is the polar angle in the $x'y'$ -plane. The sparking pattern diverges away from θ'_s and converges toward θ'_e (see Figures 4 and 5). The rate of shifting of the patterns in the two halves of each ring is estimated as $\omega_{u,d} = \mp \theta_{\text{sprk}}/P_3$.

Table 3
The Details of the Spark Distribution in the Polar Cap

	Cone	i	a_{out} (m)	a_{in} (m)	b_{out} (m)	b_{in} (m)	N_{sprk}	θ_{sprk} (deg)	a_{trk} (m)	b_{trk} (m)	$\omega_{u,d}$ (deg s ⁻¹)
J1034–3224	Outer	1	36.2	22.8	15.1	9.5	13	27.7	29.5	12.3	∓ 3.8
	Inner	2	22.8	9.4	9.5	3.9	7	51.4	16.1	6.7	∓ 7.1
J1720–2933	Outer	1	75.2	47.3	30.1	19.0	13	27.7	61.3	24.5	∓ 11.3
	Inner	2	47.3	19.5	30.1	7.8	7	51.4	33.4	13.4	∓ 21.0

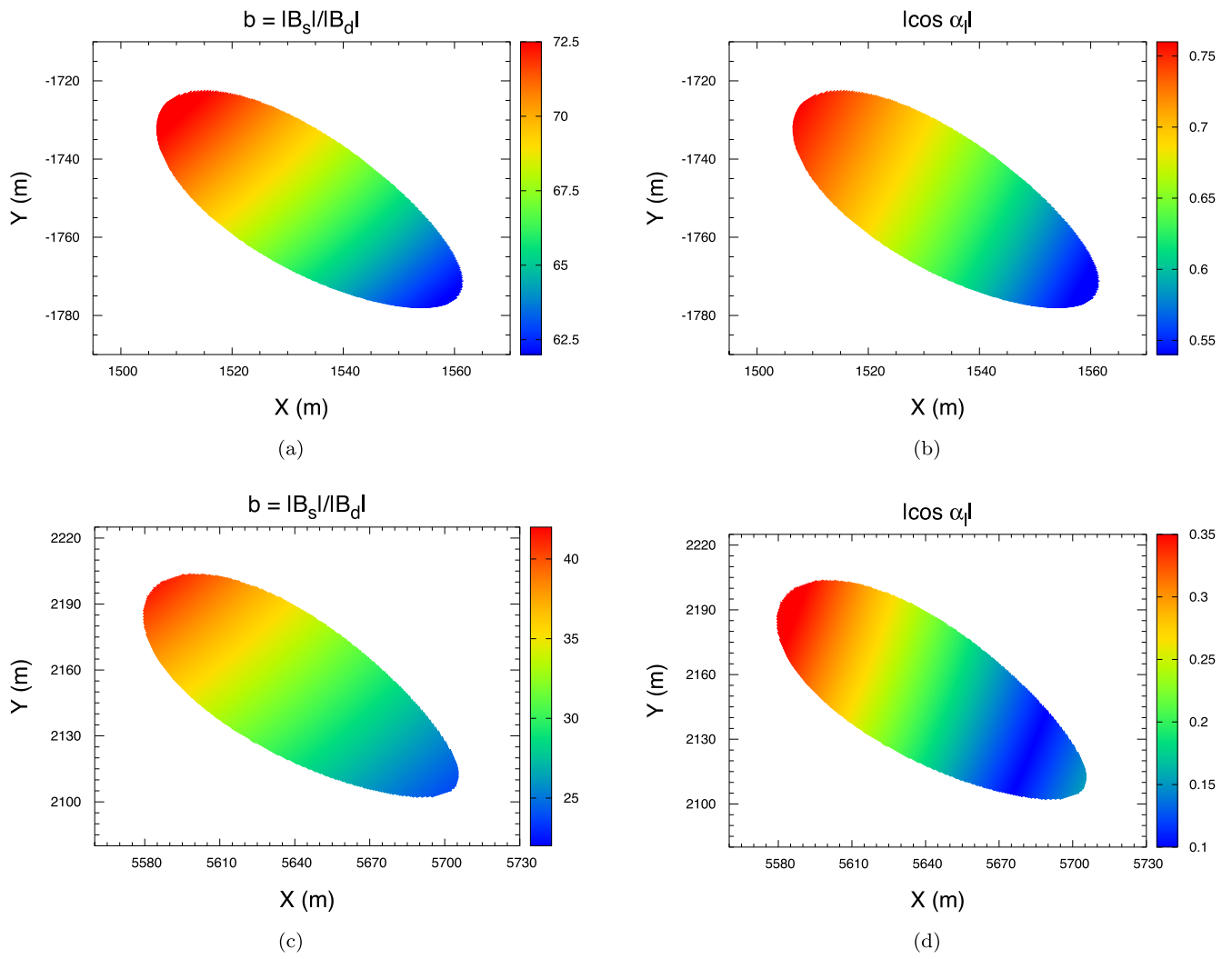


Figure 3. The physical conditions above the simulated polar caps of the two pulsars.

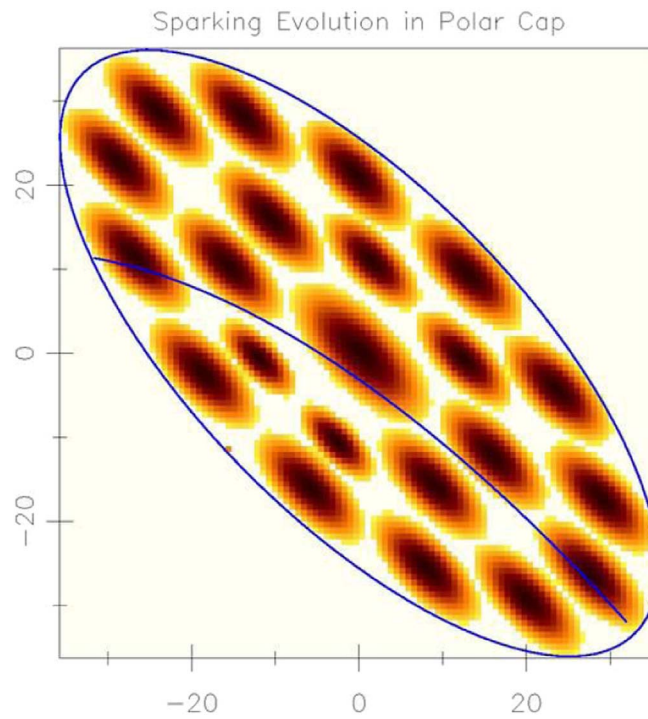


Figure 4. The two-dimensional distribution of the sparking pattern above the simulated polar cap corresponding to PSR J1034–3224. The sparks are arranged in two concentric elliptical annuli around a central spark in a tightly packed configuration. The sparking pattern evolves with time to show an anticlockwise shift in the left half and a clockwise shift in the right half bounded by the points $\theta'_s = 88^\circ.7$ and $\theta'_e = 268^\circ.6$, where the pattern shifts away from θ'_s and converges toward θ'_e . The LOS traverse across the emission beam at a relative shift $\beta = 1^\circ.6$ from the center and its imprint on the polar cap are also shown. The dynamical evolution of the spark distribution across the LOS results in bi-drifting. An animation showing the evolution of the spark configuration with time is available.

(An animation of this figure is available.)

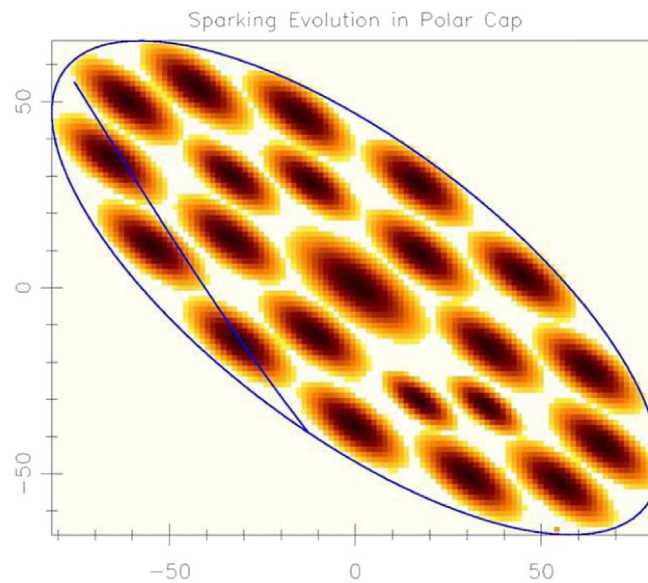


Figure 5. The two-dimensional distribution of the sparking pattern above the simulated polar cap corresponding to PSR J1720–2933. The sparks are arranged in two concentric elliptical annuli around a central spark in a tightly packed configuration. The sparking pattern evolves with time to show an anticlockwise shift in the left half and a clockwise shift in the right half bounded by the points $\theta'_s = 122^\circ.4$ and $\theta'_e = 302^\circ.4$, where the pattern shifts away from θ'_s and converges toward θ'_e . The LOS traverse across the emission beam at a relative shift $\beta = -5^\circ.4$ from the center and its imprint on the polar cap are also shown. The dynamical evolution of the spark distribution across the LOS results in coherent subpulse drifting. An animation showing the evolution of the spark configuration with time is available.

(An animation of this figure is available.)

Appendix B

Simulated Single Pulse Sequence with Subpulse Drifting

The procedure for simulating the single pulse emission, as well as estimating the LRFS to obtain the subpulse drifting behavior in the two pulsars, is described in Basu et al. (2022).

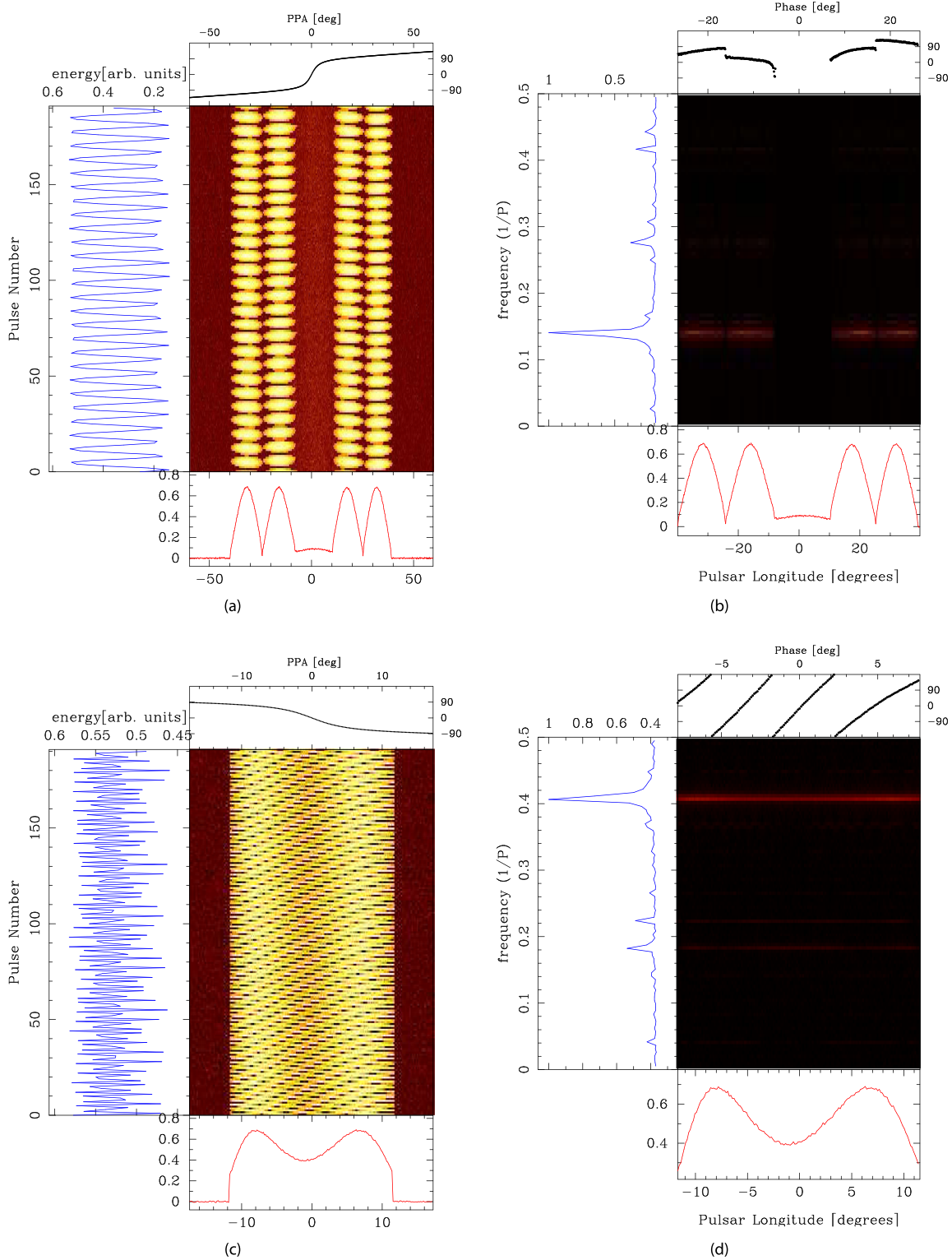





Figure 6. Single-pulse simulations demonstrating the bi-drifting behavior of PSR J1034–3224 (panels (a) and (b)) and the coherent drifting behavior of PSR J1720–2933 (panels (c) and (d)). Pulse stacks with 200 simulated single pulses are shown in panels (a) and (c), while the LRFS across the pulse window is represented in panels (b) and (d). The drifting periodicity $P_3 = 7.2P$ is seen as peak frequency $f_p \sim 0.14$ cycles/ P in panel (b), while $P_3 = 2.45P$ is seen as peak frequency $f_p \sim 0.41$ cycles/ P in panel (d). The evolution of the sparking pattern across the polar cap is reflected in the phase behavior across the profile in the right panels.

central component is not visible in the average profile, which comprises four components, matching the observations. Figure 6(c) shows around 200 pulses resembling the coherent drifting behavior in PSR J1720–2933. The LRFS in Figure 6(d) shows the frequency peak corresponding to periodic drifting and the large phase behavior across the emission window. The LOS only cuts along the outer conal track of the sparks, and the average profile shows a dip at the center, which is the observed behavior.

ORCID iDs

Rahul Basu  <https://orcid.org/0000-0003-1824-4487>
 Dipanjan Mitra  <https://orcid.org/0000-0002-9142-9835>
 George I. Melikidze  <https://orcid.org/0000-0003-1879-1659>

References

- Arumugasamy, P., & Mitra, D. 2019, *MNRAS*, 489, 4589
 Backer, D. C. 1973, *ApJ*, 182, 245
 Basu, R., Melikidze, G. I., & Mitra, D. 2022, *ApJ*, 936, 35
 Basu, R., & Mitra, D. 2018, *MNRAS*, 475, 5098
 Basu, R., Mitra, D., & Melikidze, G. I. 2020, *MNRAS*, 496, 465
 Basu, R., Mitra, D., Melikidze, G. I., et al. 2016, *ApJ*, 833, 29
 Basu, R., Mitra, D., Melikidze, G. I., & Skrzypczak, A. 2019a, *MNRAS*, 482, 3757
 Basu, R., Mitra, D., & Rankin, J. M. 2015, *ApJ*, 798, 105
 Basu, R., Paul, A., & Mitra, D. 2019b, *MNRAS*, 486, 5216
 Champion, D. J., Lorimer, D. R., McLaughlin, M. A., et al. 2005, *MNRAS*, 363, 929
 Geppert, U. 2017, *JApA*, 38, 46
 Gil, J. A., Melikidze, G. I., & Mitra, D. 2002, *A&A*, 388, 235
 Gil, J., Gronkowski, P., & Rudnicki, W. 1984, *A&A*, 132, 312
 Gil, J., Haberl, F., Melikidze, G., et al. 2008, *ApJ*, 686, 497
 Gil, J., Melikidze, G. I., & Geppert, U. 2003, *A&A*, 407, 315
 Hermsen, W., Hessels, J. W. T., Kuiper, L., et al. 2013, *Sci*, 339, 436
 Hermsen, W., Kuiper, L., Basu, R., et al. 2018, *MNRAS*, 480, 3655
 Kijak, J., & Gil, J. 1998, *MNRAS*, 299, 855
 Krzeszowski, K., Mitra, D., Gupta, Y., et al. 2009, *MNRAS*, 393, 1617
 Mitra, D. 2017, *JApA*, 38, 52
 Mitra, D., Basu, R., Maciesiak, K., et al. 2016, *ApJ*, 833, 28
 Mitra, D., Basu, R., Melikidze, G. I., & Arjunwadkar, M. 2020, *MNRAS*, 492, 2468
 Mitra, D., & Deshpande, A. A. 1999, *A&A*, 346, 906
 Mitra, D., & Li, X. H. 2004, *A&A*, 421, 215
 Mitra, D., & Rankin, J. M. 2002, *ApJ*, 577, 322
 Pétri, J., & Mitra, D. 2020, *MNRAS*, 491, 80
 Radhakrishnan, V., & Cooke, D. J. 1969, *ApL*, 3, 225
 Rankin, J. M. 1993, *ApJ*, 405, 285
 Ruderman, M. A., & Sutherland, P. G. 1975, *ApJ*, 196, 51
 Shang, L.-H., Bai, J.-T., Dang, S.-J., & Zhi, Q.-J. 2022, *RAA*, 22, 025018
 Skrzypczak, A., Basu, R., Mitra, D., et al. 2018, *ApJ*, 854, 162
 Song, X., Weltevrede, P., Szary, A., et al. 2023, *MNRAS*, 520, 4562
 Szary, A., Gil, J., Zhang, B., et al. 2017, *ApJ*, 835, 178
 Szary, A., & van Leeuwen, J. 2017, *ApJ*, 845, 95
 Szary, A., van Leeuwen, J., Weltevrede, P., & Maan, Y. 2020, *ApJ*, 896, 168
 Sznajder, M., & Geppert, U. 2020, *MNRAS*, 493, 3770
 von Hoensbroech, A., & Xilouris, K. M. 1997, *A&AS*, 126, 121
 Weltevrede, P. 2016, *A&A*, 590, A109
 Weltevrede, P., Edwards, R. T., & Stappers, B. W. 2006, *A&A*, 445, 243
 Weltevrede, P., & Johnston, S. 2008, *MNRAS*, 391, 1210